

RESEARCH ARTICLE | AUGUST 14 2023

Sputtering of amorphous Si by low-energy Ar⁺, Kr⁺, and Xe⁺ ions

D. R. Shibanov   ; D. V. Lopaev   ; S. M. Zyryanov  ; A. I. Zotovich  ; K. I. Maslakov  ; A. T. Rakhimov

 Check for updates

Journal of Applied Physics 134, 063304 (2023)

<https://doi.org/10.1063/5.0160531>



View Online



Export Citation

CrossMark

Articles You May Be Interested In

Precise ion energy control with tailored waveform biasing for atomic scale processing

Journal of Applied Physics (December 2020)

Innovative remote plasma source for atomic layer deposition for GaN devices

Journal of Vacuum Science & Technology A (September 2021)

Discharge physics and atomic layer etching in Ar/C₄F₆ inductively coupled plasmas with a radio frequency bias

Physics of Plasmas (June 2021)



Optimize Your Research

New Vacuum Gauge Provides More Process Control and Operational Reliability



Sputtering of amorphous Si by low-energy Ar⁺, Kr⁺, and Xe⁺ ions

Cite as: J. Appl. Phys. **134**, 063304 (2023); doi: 10.1063/5.0160531

Submitted: 2 June 2023 · Accepted: 26 July 2023 ·

Published Online: 14 August 2023



D. R. Shibano^{1,a)}  D. V. Lopaev^{1,a)}  S. M. Zyryanov¹  A. I. Zotovich¹  K. I. Maslakov²  and A. T. Rakhimov¹

AFFILIATIONS

¹Lomonosov Moscow State University, Skobeltsyn Institute of Nuclear Physics, Moscow, Russia

²Department of Chemistry, Lomonosov Moscow State University, Moscow, Russia

^{a)}Authors to whom correspondence should be addressed: danshibanov@gmail.com and d.lopaev@gmail.com

ABSTRACT

Atomic layer plasma technologies require localizing ions' impact within nanometers up to an atomic layer. The possible way to achieve this is the decrease in the ion energy up to surface binding energy. At such low ion kinetic energies, the impact of different plasma effects, causing the surface modification, can be of the same order as kinetic ones. In this work, we studied the sputtering of amorphous silicon films by Ar⁺, Kr⁺, and Xe⁺ ions at energies of 20–200 eV under the low-pressure inductively coupled plasma discharge in pure argon, krypton, and xenon, respectively, at a plasma density of $1\text{--}1.5 \times 10^{10} \text{ cm}^{-3}$. Under the plasma conditions, a high asymmetry of discharge allowed to form ion flux energy distribution functions with narrow energy peak ($5 \pm 2 \text{ eV}$ full width at half maximum). Real time *in situ* control over the ion composition and flux as well as the sputtering rate (the ratio of the film thickness change to the sputtering time) provided accurate determination of the sputtering yields $Y(E_i)$. It is shown that at ion energy above $\sim 70 \text{ eV}$, the “classical” kinetic sputtering mechanism prevails. In this case, $Y(E_i)$ grows rather rapidly with ion energy, increasing with the decrease in the ion mass: the closer the ion mass to the target atom mass, the higher the $Y(E_i)$. Below 70 eV, the growth of $Y(E_i)$ strongly slows down, with $Y(20 \text{ eV})$ being still high ($>10^{-3}$), indicating the impact of plasma. The obtained trends of $Y(E_i)$ are discussed in light of surface modification studied by atomic force microscopy and angular x-ray photoelectronic spectroscopy.

Published under an exclusive license by AIP Publishing. <https://doi.org/10.1063/5.0160531>

I. INTRODUCTION

The interaction of energetic ions with matter has been studied for more than a hundred years, but it still attracts more attention, being highly important in various fields of science and technology such as microelectronics, space research, radiation safety, and ion-beam medicine.^{1–3} Physics of high-energy ions' impact (with an energy of $\gtrsim 1 \text{ keV}$) on materials has been studied in detail.^{4,5} The mechanism of such interaction is generally well understood and described within the framework of quasi-classical approaches and is often called a “kinetic” mechanism, since purely kinetic effects are predominant at these energies. Being, to some extent, the generalization of such a classical kinetic approach, the world-famous TRIM package provides reliable predictions of ion-material interactions for high-energy ions.⁶

However, in modern microelectronic technology, the transition to the atomic scale era requires localizing ions' impact within one atomic layer. The application of ultra-low energetic ions (5–50 eV), with energy to be of the order of atoms' binding energy,

into manufacturing processes such as PEALE (plasma enhanced atomic layer etching) and PEALD (plasma enhanced atomic layer deposition) is necessary to reach the requirement. At such low ion kinetic energies, the impact of potential effects, both the surface restructuring (i.e., modification) and electronic excitation through ion neutralization, can be of the same order as kinetic ones. While molecular dynamics is better suited for the calculations of sputtering for low-energy ions than the TRIM package, it is still unable to directly reckon for any quantum-mechanical effects as well as long-time macroscopical effects and overall requires validations by reliable experimental data. At the same time, *ab initio* quantum-mechanical calculation methods are severely limited by modern computational capabilities for the sputtering calculations.

Nevertheless, at present, there is a sufficiently extensive set of data on the sputtering of different materials by different types of ions,⁷ and an overwhelming majority of the studies have been carried out with ion beams (often of high energy of several hundreds of eV and higher). Thus, there are almost no reliable data on

22 August 2023 09:06:09

the ion sputtering yield [$Y(E_i)$ is defined as the probability of a target atom to leave the surface per coming ion with kinetic energy E_i] at ion energies below 100 eV, even for such an important material for microelectronic applications as silicon. The reason for that is almost entirely associated with technical difficulties such as the generation of dense spatially homogeneous ion beams of such low energies with small energy and angular dispersion, and accurate measurement of very low values of yield. Moreover, in standard beam experiments, the yield and ion energy errors grow as the ion energy decreases and, at tens of electron volts, become comparable with the values and may even overcome them several times. Therefore, it is not surprising that the $Y(E_i)$ data obtained by different authors at $E_i < 100$ eV often differ by more than an order of magnitude.

At the same time, in low-temperature plasma, the formation of a uniform dense flux with small angular and energy dispersions on a large-area surface is not an issue nowadays, even for low-energy ions. Surely, plasma usage for sputtering studies has its own peculiarities and disadvantages (limitation on angle of incidence, redeposition, etc.), which must be considered in detail in sputtering results' discussion, yet, in the plasma case, the study of sputtering takes place under conditions as close as possible to real plasma technological processes.

In this work, the sputtering of thin films of amorphous silicon by low-energy Ar^+ , Kr^+ , and Xe^+ ions in the range of 20–200 eV was studied in low-pressure inductively coupled plasma (ICP) plasma in pure argon, krypton, and xenon, respectively. Sputtering rate (the ratio of the film thickness change to the sputtering time) measurements were made *in situ* with a laser ellipsometer, while various plasma diagnostics were used to accurately determine the composition, energy spectrum, and ion flux onto a sample surface. The surface modification of Si films during sputtering was determined by *ex situ* surface diagnostics: vacuum atomic force microscopy (AFM) and angular x-ray photoelectron spectroscopy (XPS). It was shown that sputtering still preserves at ion energies below the kinetic sputtering threshold. However, the dependence $Y(E_i)$ drastically changes at the energy of about ~ 75 eV. The role of plasma effects on the sputtering mechanism, as well as potential sputtering itself at low ion energies, would be discussed in Sec. IV of the work.

This work is organized as follows: the experiment is described in detail in Sec. II, Sec. III presents the results obtained and a brief discussion of them, and the conclusion is given in Sec. IV.

II. EXPERIMENTAL SETUP

A. Plasma chamber and discharge parameters' overview

The experimental study was divided into three parts.

- (1) Study of Ar, Kr, and Xe plasmas in detail at different pressures, gas flows, and applied powers to define the most suitable regimes for the sputtering.
- (2) Sputtering of Si samples at the selected regimes with *in situ* control of both sputtering and plasma parameters,
- (3) *Ex situ* investigation of the treated and pristine samples by AFM and angular XPS.

The experiments were carried out in a dual frequency radio frequency (df rf) ICP discharge chamber shown in Fig. 1. The chamber was a grounded metallic cylinder 35 cm in diameter and 10 cm in height. The chamber top lid had an opening 19 cm in diameter in the center, covered by a 20 cm in diameter silica plate. The plasmas were inductively driven at 13.56 MHz by a three-turn spiral coil, placed above the silica plate. The coil was 19 cm in diameter and was made from a copper pipe 1.6 cm in diameter. A grounded electrostatic screen was placed between the plate and the coil. Silicon samples were placed on top of the aluminum electrode, placed at the bottom of the chamber. The electrode was rf-biased at 12 MHz through a blocking capacitor to provide self-bias. Waveforms of floating potential V_{dc} and bias voltage V_{bias} on the electrode were real time measured by an oscilloscope and rf data acquisition system (rf-QAQ). A thermal contact between the electrode and samples was provided by thermal paste. The electrode and the coil were cooled by flowing water of about 16–17 °C for thermal stability. The chamber's walls were thermally stabilized at 40 °C by a tape heater, covering them from the outside of the chamber. All of this provided stable, reproducible vacuum and plasma conditions for a very long time.

Two well-known probe diagnostics were used to determine and control plasma parameters.

- (1) The rf-compensated Langmuir probe was used to measure plasma and floating potentials (also controlled by a special measurement circuit), as well as the electron energy distribution function (EEDF).^{7,8} Since the EEDFs in all chosen discharge regimes were almost Maxwellian ones, it allowed determining accurately electron temperature T_e , needed for estimating ion flux on a sample surface. In addition, the plasma density n_e , estimated on the integrated electron energy probability function (EEDF), was compared with n_e , measured by an MW hairpin probe to validate the measurements.
- (2) The microwave (MW) U-shaped hairpin probe^{9–11} was used to measure directly the electron density. The hairpin probe measurements were corrected on the sheath areas around the probe

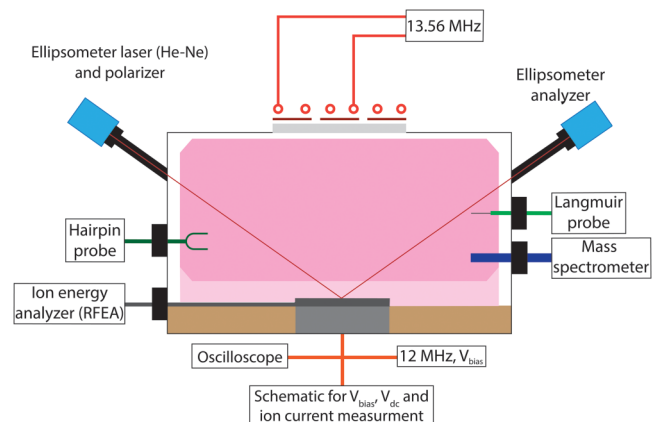


FIG. 1. Experimental setup.

22 August 2023 09:06:09

tips, assuming T_e from the Langmuir probe measurements.¹² In the considered plasma conditions, this correction is very small and does not exceed a few percent on the value of plasma density. The hairpin probe was used for continuous monitoring of the plasma density during sputtering to ensure the constancy and reproducibility of the plasma state.

The Langmuir probe's tip was made from tungsten wire of 90 μm diameter and 14 mm length. The hairpin probe's antenna was made from tungsten wire of 200 μm diameter, the distance between the tips of the hairpin probe was 12 mm, and the tip length was 5 cm. Both probes were placed at about 3 cm directly above the electrode in the quasi-neutral plasma out of the plasma sheath. The Langmuir probe was extruded from the chamber after the first part of the experiment, while the hairpin probe continuously measured the plasma density to monitor ion flux during sputtering.

The gas flows and pressure, plasma density, floating potential, bias voltage waveform, ions' mass spectra, and flux density were *in situ* measured during the first two parts of the experiment to assure the discharge parameter constancy.

The aim of the first part of the experiment was to determine the plasmas' parameters, at which the ion flux energy distribution with narrow enough energy peaks (5 ± 2 eV full width at half maximum) at each energy for all the studied gases. Since the resonant charge exchange cross section for Xe is several times larger than that for Ar and Kr (that leads to the collisional broadening of the energy distribution), the Xe pressure was lowered to preserve the desirable ion flux energy distribution. Chosen discharges' parameters for the sputtering part of the experiment are shown in Table I. Sputtering ion energies E_{ion} were 18 eV for Xe and Kr, 22 eV for Ar plasmas (no rf bias), and 25, 50, 75, 100, 125, 150, 175, and 200 eV for all three gases (with rf bias). The lowest energies were determined by the floating potential of plasmas' self-bias.

B. Ion flux

1. Ionic composition

Since the experimental chamber did not have a vacuum load port, it was fully opened at atmospheric pressure each time a sample was changed; thus, the chamber absorbed significant amounts of atmospheric gases (especially, water vapor), which could drastically change the discharge. Thereby, a long chamber cleaning in the plasma of the respective gas was applied to resolve this issue every time the sample was changed. During the cleaning procedure, the sample was at floating potential [ion energy was about 20 eV (see below)].

TABLE I. Discharges' pressure and electron plasma density.

Gas	Pressure, P (mTorr)	Electron plasma density, n_e (cm^{-3})	Electron temperature, T_e (eV)
Argon	10	1.47×10^{10}	4.7
Krypton	10	1.15×10^{10}	4
Xenon	5	1.25×10^{10}	3.5

The hidden analytical quadrupole mass spectrometer with energy analyzer was used to control *in situ* the discharge chemical composition during the first two parts of the experiment. The EQP inlet was placed at about 3 cm above the electrode in the quasi-neutral plasma out of the plasma sheath. For thermal stability and chemical stability, the mass spectrometer was heated by the tape heater up to 60 $^{\circ}\text{C}$, while its vacuum pumps were air cooled to a room temperature of about 25 $^{\circ}\text{C}$.

Just after discharge ignition (i.e., after changing sample), the concentration of contaminants in the gas composition in the chamber was very low ($<0.01\%$), while the ion composition contained more contaminants (typically H_2O^+ , H_3O^+ , N_2^+ , and O_2^+), which is a typical situation for chambers without vacuum load ports. Plasma cleaning was performed until the total amount of all undesirable admixtures' ions became strongly below 1%, which typically required about 2–3 h. Ion mass spectra of used plasmas, shown in Fig. 2, were almost constant during sputtering processes.

2. Ion flux distributions

a. Energy distribution measurement. The ion flux energy distribution function (IFEDF) on the surface of the rf-biased electrode was measured by the rf-compensated retarded field energy analyzer (RFEA),^{8,13–18} with the ion energy measurement accuracy of ~ 0.5 eV. Being the same diameter and height as the aluminum electrode, the analyzer replaced the electrode during the measurements. The analyzer measurement's area diameter was 10 mm, and the analyzer consisted of a top aluminum plate (thickness 0.8 mm) with orifices (diameter 0.8 mm), three (entrance G_0 , ion energy analyzing G_1 , and electron rejecting G_2) nickel grids ($17 \times 17 \mu\text{m}^2$ cells with an open window of $10 \times 10 \mu\text{m}^2$, 0.3 mm separation between the grids), and a beryllium copper collector plate C (see Fig. 3). Measurement and control circuits of the analyzer were separated from the grids rf filters (rf chokes). The RFEA was water cooled during all the measurements for thermal stability.

After the IFEDFs were measured, the RFEA was replaced by the electrode of the same thickness, on which the silicon samples were placed during sputtering. Since both electrode configuration and all plasma parameters were the same during the IFEDFs' measurements and the sputtering, it is assumed that real IFEDFs of ions bombarding the samples matched with measured ones. However, to assure that, some additional investigations were made (see Secs. II B 2 c and II B 2 d of the current chapter).

b. IFEDF control. As known,^{8,19,20} in the low-pressure asymmetrical CCP rf discharge, driven by sinusoidal voltage, the IFEDF has a classical bimodal distribution, centered approximately around the energy of $eU_{sh} = e(U_p - U_{dc})$ (where U_{sh} is the plasma sheath voltage, U_p is the plasma potential, and U_{dc} is the negative dc self-bias), with the distribution width increasing with the bias voltage increase and plasma density decrease [Figs. 4(a) and 4(b)]. The bimodal structure reflects the ion response to the sheath voltage waveform. The IFEDFs at constant mean ion energy could be narrowed by increasing.

(a) The rf frequency at constant plasma density (i.e., constant sheath thickness).

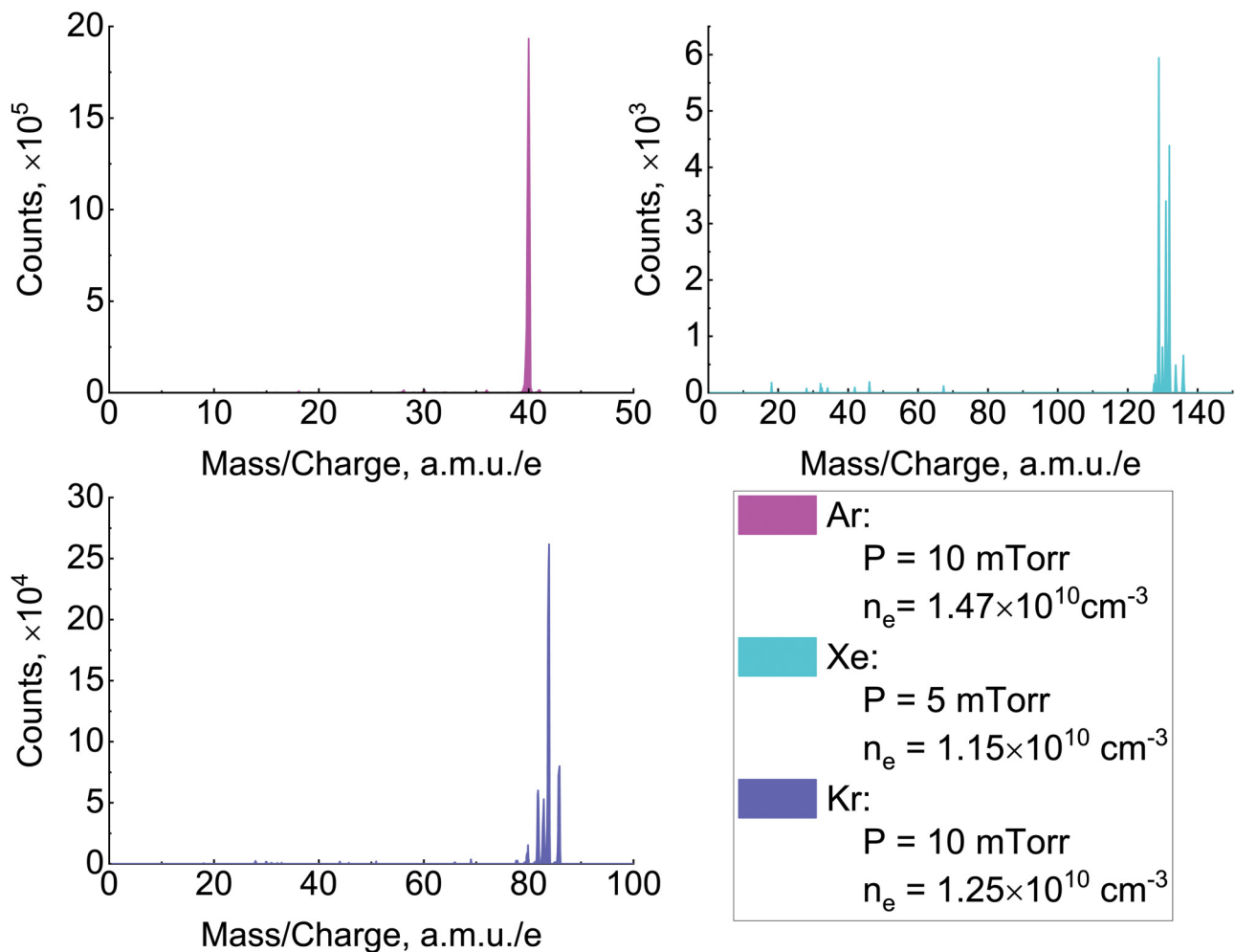


FIG. 2. Mass spectra of argon, xenon, and krypton collisionless plasmas.

(b) The plasma sheath thickness at constant rf frequency (i.e., decreasing plasma density).

However, the decrease in the plasma density, i.e., the ion flux, is undesirable at low ion energy as it leads to the essential decrease in the sputtering rate, making measurements very long and less reliable.

The usage of an optimal tailored waveform of rf bias as, for example, in Faraz *et al.*²¹ allows forming quite narrow pick IFEDFs and, therefore, provides precise ion energy control. The similar results can also be achieved, when the rf bias voltage is only somewhat different from the sinusoidal. In a strongly asymmetric ICP discharge, plasma impacts on the plasma sheath nearby the electrode, which leads to the appearance of the negative dc bias. The higher the asymmetry between plasma sheaths, the stronger this impact (note that there is no negative dc bias in a fully symmetrical rf discharge). Due to the asymmetry, the sheath non-linearity leads to the appearance of rf harmonics on the rf-biased electrode, which

provides the non-sinusoidal voltage. In low-density plasma with thick plasma sheath and pre-sheath, this difference is small and, therefore, the voltage at the electrode almost copies the shape of the applied sinusoidal voltage from the rf generator. On the contrary, in relatively dense plasma with a thinner sheath, the shape of the bias at the electrode is a sum of the biasing voltage and its harmonics generated in the plasma. The resulting bias may be similar to a tailored voltage waveform and also leads to a strong asymmetry in the IFEDF shape. The resulting bias waveform and, correspondingly, the caused asymmetry depend on both plasma conditions and discharge geometry. The denser the plasma, the thinner the sheath and, thus, the wider the IFEDF and the higher the asymmetry in peaks of the bimodal distribution. Considering all the above, one of the aims of our study was to select such discharge parameters, at which the plasma sheath is collisionless (even at high biases) but still thin enough to provide a strong asymmetry in the IFEDF peaks and, therefore, more precise control over ion's energy.

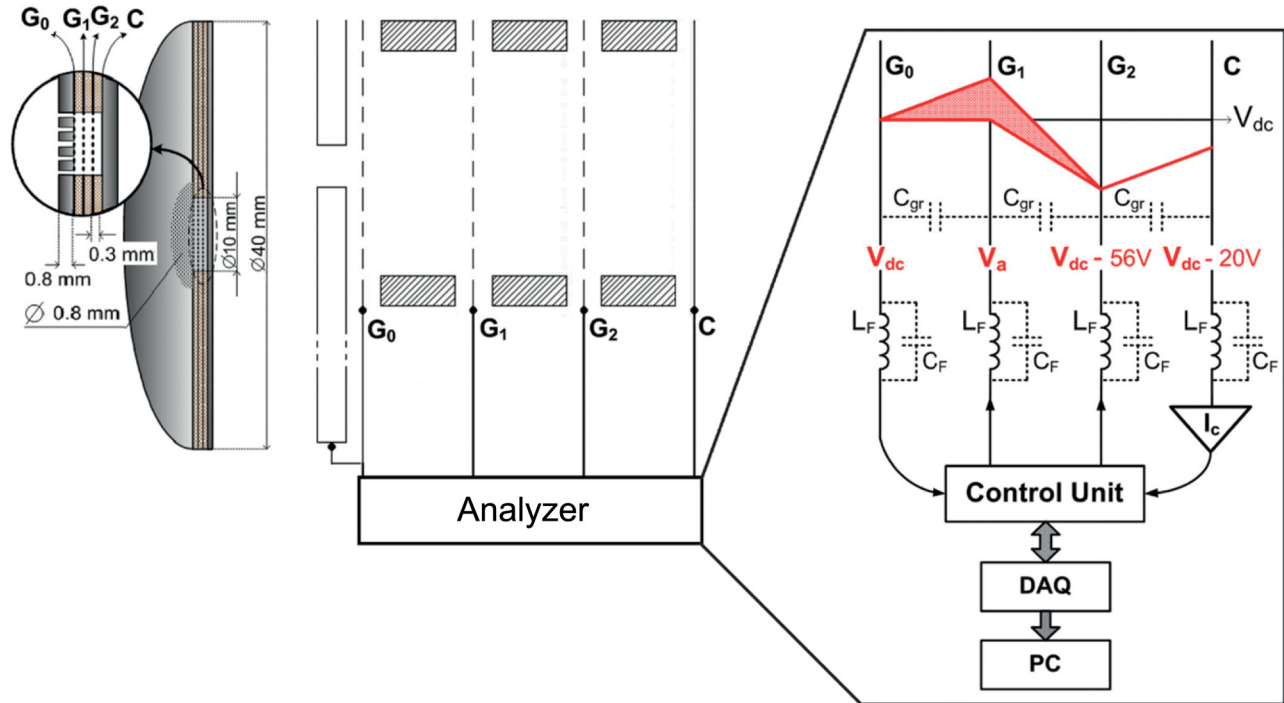


FIG. 3. RFEA scheme.

Figures 4(c) and 4(b) illustrate the measured resulting bias waveform at the electrode and corresponding IFEDFs, respectively. As seen, the low-energy peak was effectively depressed, and IFEDF looks as mono-energetic distribution with $(\delta E_i/E_i) \sim 10\%$ (where E_i is the energy of the high-energy peak and δE_i is the FWHM of the peak).

c. Sample influence on ions' energy. The energy of ions bombarding a sample can differ from the ion energy measured by RFEA, if the sample is not a good conductor similar to metal. Voltage drops over the sample and plasma sheath can be estimated by comparing samples' capacitance with the characteristic capacitance of the plasma sheath. Voltage drop and sheath's capacitance at the lowest and highest ions' energies for each gas discharge are shown in Table II. The sheath's capacitance was calculated by estimating the sheath's thickness from Child–Langmuir's law.²² The presented data demonstrate that the voltage drop over the sample is small enough to assume that the ions' energies measured by the RFEA and the energies of the ions bombarding the sputtered samples were the same.

d. Ion angular distribution. As known,²³ the sputtering rate depends on ions' angle of incidence. Up to a certain angle, depending on ions' energy and type, material structure, and composition, the sputtering rate increases with the angle deviation from normal incidents. Thus, it is important to at least estimate real ion angular distribution under plasma conditions.

Passing through a pre-sheath, ions accelerate to the electrode, increasing their kinetic energy kT_i in plasma bulk ($T_i > T_g$, where T_g is the gas temperature) up to $kT_e/2$, while they may collide with neutrals and ions due to the large dimension of the pre-sheath even at low pressures of this work. At the same conditions, the sheath is almost collisionless; thus, the bias voltage accelerates ions without scattering. Thereby, the ion angular distribution is characterized by the ratio of the average kinetic energy of the ions' motion (parallel to the electrode $kT_{i\perp}$ and obtained in the pre-sheath) to the energy of the ions' acceleration to the electrode in the sheath E_{ion} (since $kT_e/2 \ll E_{ion}$). In this work, the pre-sheath is weakly collisional and, therefore, $kT_{i\perp}$ is strongly less than $kT_e/2$. Considering all the above, the ion angular distribution can be estimated as deviation from normal incidence $\delta\Omega = \sqrt{kT_{i\perp}/E_{ion}}$ as an interval: $\sqrt{kT_g/E_i} < \delta\Omega < \sqrt{kT_e/2E_i}$, presented in Table III. Note that, since the pre-sheath is slightly collisional, the center of the ion angular distribution is much closer to $\sqrt{kT_g/E_i}$ than to $\sqrt{kT_e/2E_i}$; i.e., $\sqrt{kT_g/E_i} < \delta\Omega \ll \sqrt{kT_e/2E_i}$ is valid, and $\delta\Omega$ is only a few of degrees even at the lowest energy.

3. Ion flux measurement

a. Self-bias technique. The ion flux to the sample's surface can be measured by the RFEA as done in Refs. 13–16 if the RFEA was absolutely calibrated in the correct way. If the calibration was done under the same plasma conditions, the result is correct. However, if the calibration was done the other way

22 August 2023 09:06:09

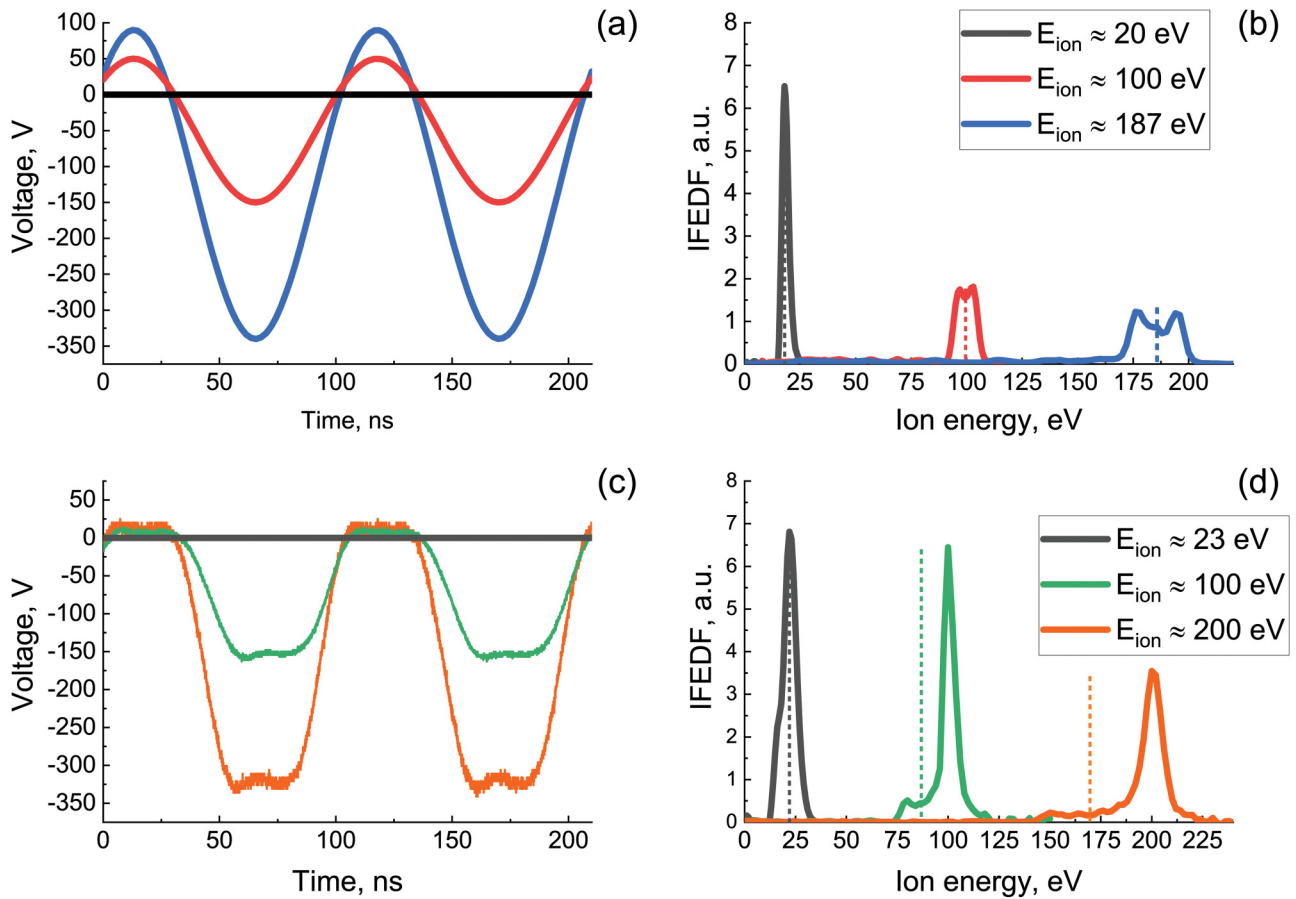


FIG. 4. (a) and (c) Bias voltage waveforms and (b) and (d) ion flux energy distribution functions (IFEDFs) for the biases, corresponding to voltages at (a) and (c) accordingly, in collisionless argon plasma. (a) and (b) correspond to classical asymmetrical discharge with sinusoidal bias voltage waveform ($P = 10$ mTorr, $n_e \approx 1 \times 10^9$ cm $^{-3}$), while (c) and (d) show the bias waveform and IFEDF in the given experiment ($P = 10$ mTorr, $n_e = 1.47 \times 10^{10}$ cm $^{-3}$). Dot lines illustrate the energy corresponding to the dc bias voltage $eU_{sh} = e(U_p - U_{dc})$.

22 August 2023 09:06:09

TABLE II. Plasma sheath capacitance and voltage drop on the sample.

	P (mTorr)	n_e (cm $^{-3}$)	E_{ion} (eV)	R_{Debye} (cm)	S_{sheath} (cm)	C (pF/cm 2)	Voltage drop (%)
Ar	10	1.4×10^{10}	50	0.0137	0.158	34	2.52
			100	0.0135	0.251	22	1.60
			200	0.0123	0.396	14	1.02
Xe	5	1.15×10^{10}	50	0.0131	0.172	32	2.33
			100	0.0126	0.224	24	1.80
			200	0.0127	0.457	12	0.89
Kr	10	1.25×10^{10}	50	0.0133	0.169	32	2.36
			100	0.0127	0.290	19	1.39
			200	0.0123	0.468	12	0.86

(using ion beam, for example), this approach may be rather unreliable, since the grid alignment together with the electrical fields' distribution between them and the effect of the ion angle distribution is able to unpredictably impact on the RFEA grid transparency¹⁷ and, therefore, the ion current (i.e., demanding absolute re-calibration for each change in ions' energy or discharge's parameters).

TABLE III. Deviation from normal incidence for each processing gas at different ion energies.

	$\delta\Omega$ at $E_{ion} = 50$ eV	$\delta\Omega$ at $E_{ion} = 200$ eV
Ar	0.8°–12.5°	0.75°–6.2°
Xe	0.8°–11.5°	0.75°–5.7°
Kr	0.8°–10.7°	0.75°–5.4°

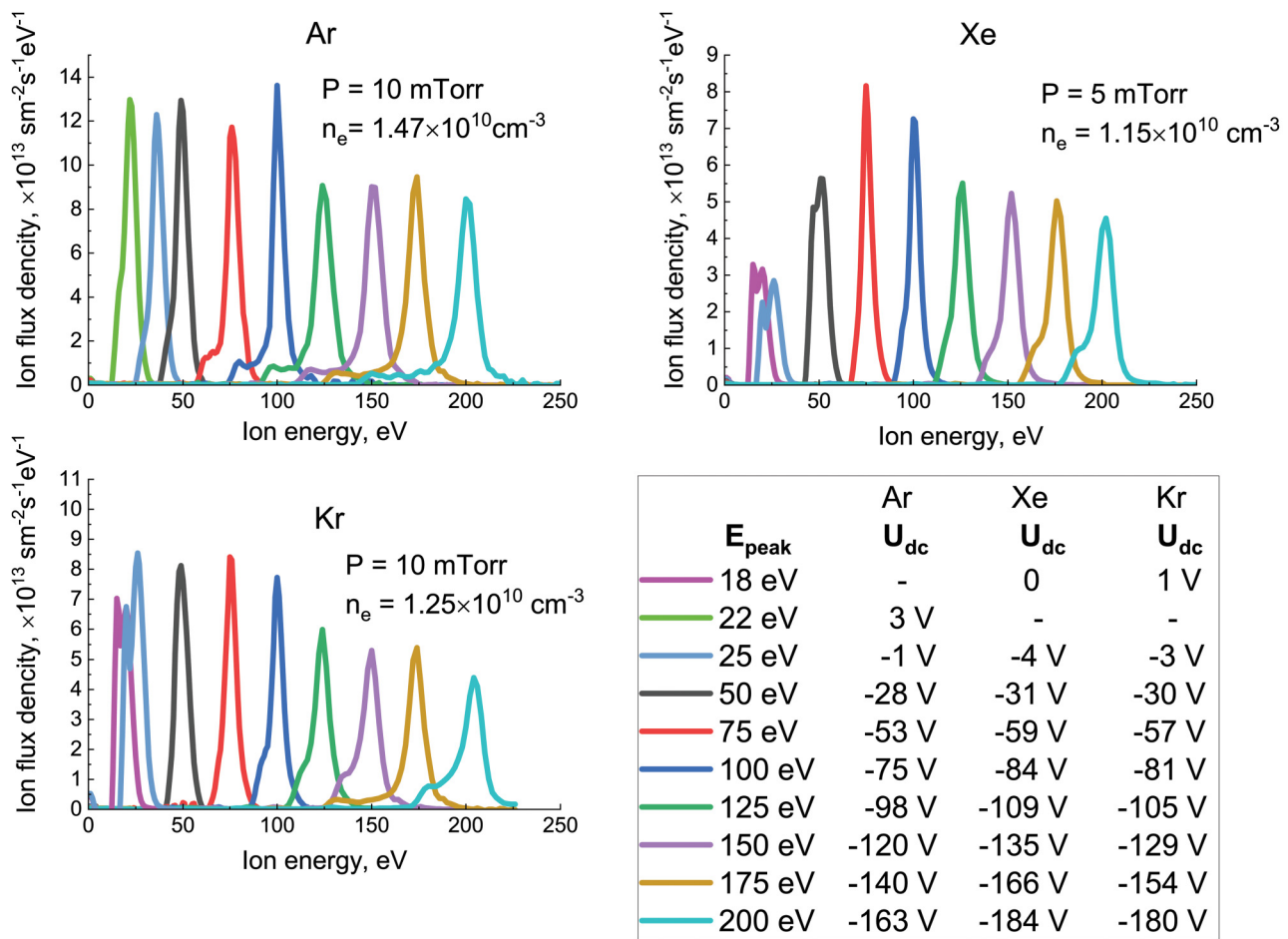


FIG. 5. Ion flux density dependence on the bias voltage applied to the electrode for Ar, Xe, and Kr discharges.

Thus, in this work, the absolute measurements of the ion current were made using a rf bias modulation technique,^{8,18,24} well applicable for the asymmetric rf discharges. The main idea of this method is to use an electric charge, accumulated in the blocking capacitor, to measure the ion current. For plasma's ions, the rf bias voltage charge the capacitor to the negative dc bias, therefore, turning off the rf bias causes the blocking capacitor to be gradually recharged by ion current up to floating potential. Measuring current and voltage dependencies over time during the recharge provides data necessary for ion flux determination (for the measurements to be correct, the recharge duration should greatly surpass the turning off process duration). The process volt-ampere characteristics $I(V_{\text{bias}})$ provide the correct determination of the ion flux: $F_{\text{ion}} = I_i/eS$ (where I_i is the measured ion current, e is the electron charge, and S is the electrode area). The measured IFEDFs normalized to the measured ion current in pure Ar, Xe, and Kr at constant plasma density (see Table I) are shown in Fig. 5.

b. Calculation from plasma parameters. The ion flux can be calculated using the well-known expression:²² $F_{\text{ion}}^{\text{plasma}} = kV_{\text{Bohm}}n_e$,

where k is the collection coefficient, $V_{\text{Bohm}} = \sqrt{kT_e/M_i}$ is the Bohm velocity, and n_e is the electron plasma density. The collection coefficient k : $k = F_{\text{ion}}/V_{\text{Bohm}}n_e$, where F_{ion} is the ion flux measured by the self-bias modulation method and n_e is the plasma density. The resulting coefficients ($k_{\text{Ar}} = 0.38 \pm 0.03$, $k_{\text{Kr}} = 0.30 \pm 0.02$, and $k_{\text{Xe}} = 0.32 \pm 0.02$ for argon, krypton, and xenon discharges, respectively) are in good accordance with the study for corresponding gases²⁴ and different analytical and numerical models of the flat plasma sheath.

C. Silicon samples

1. Atomic force microscopy

a. Samples' structure. Studied silicon samples were pieces ($\approx 1 \times 2 \text{ cm}^2$) of a magnetron deposited thin film ($\approx 150 \text{ nm}$) of amorphous silicon on top of a silicon dioxide film ($\approx 600 \text{ nm}$) deposited from TEOS in the PECVD process on a silicon substrate ($\approx 0.8 \text{ mm}$) (Fig. 6). During sputtering, each sample was fixed by a

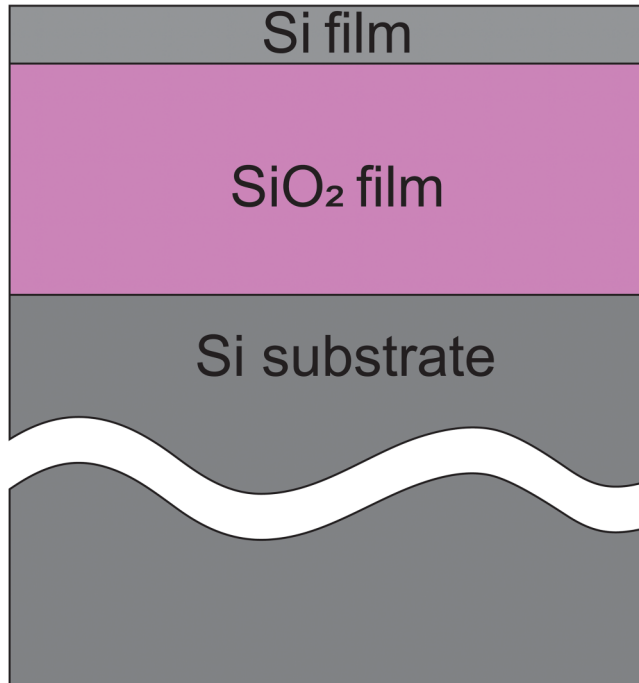


FIG. 6. Scheme of the silicon samples.

thermal paste on the water-cooled biased electrode for thermal stability.

b. AFM study. Since the sputtering rates depend on the ions' angle of incidence, the sample's surface roughness may noticeably affect the rates. Moreover, the surface roughness may also change during sputtering. Thus, after sputtering ~ 20 nm by the 200 eV ions, the surface roughness of pristine samples was studied by vacuum atomic force microscopy (AFM). AFM scans in Fig. 7 demonstrate a significant decrease (from about ± 2 – 3 nm at the pristine surface to about ± 0.5 – 0.75 nm) in the silicon sample's surface roughness after sputtering. To flatten the sample surface and remove any possible contamination (contaminated and oxidized layers, absorbed molecules, etc.) after every sample change, the measurements started from 40 to 120 min sputtering ~ 20 nm of the top layer by 200 eV energy ions of processing gas. The samples were sputtered by ions with different energies in a single process, decreasing ion energy step by step from 200 eV to no-bias corresponding energy and sputtering 10–15 nm for each ion energy to avoid any "artifacts" after the previous energy impact.

2. XPS study

According to the AFM study, ions can change material roughness, i.e., modify the structure of the top layer of the material. Besides sputtering, bombarding ions also penetrate the sample material, causing the destruction of the initial atomic structure of the material, while some ions are stuck in the material. The XPS

study was applied to try to figure out how the sputtering varies the subsurface layer of silicon.

The angular XPS studies were carried out using Kratos Analytical Axis Ultra DLD, while angular dependencies were obtained in the electrostatic lens mode, counting the angle of incident from a sample surface (90° corresponds to a normal to the surface incidence). Since the angular XPS analysis is a very time-consuming technique and krypton ion sputtering rates lay between argon and xenon ones, to catch main physical tendencies in appropriate time, krypton ion sputtered samples were excluded from the studies. The obtained XPS spectra will be discussed in the discussion section of that paper.

3. Ellipsometry

Measurements of sputtered thickness dynamics necessary to determine the sputtered rate (the ratio of the film thickness change to the sputtering time if the sputtering process is linear) were made by *in situ* ellipsometry.^{25,26} A Sentech SE800 spectroscopic ellipsometer was used to measure the film thickness and refractive index before and after sputtering, while the *in situ* film thickness and refractive index at 632.8 nm measurements were made by a Sentech SE401 laser ellipsometer. The presence of the underlying SiO₂ layer dividing the deposited Si from the silicon substrate enabled to determine quite accurately the parameters of the Si layer.

While the measurements from both ellipsometers matched, the laser ellipsometry data were used only to determine the sputtered thickness as a change in the film thickness during the process. The instrumental measurement accuracy of the thickness change was about ± 0.5 Å and of time was ± 0.5 s. An example of laser ellipsometry measurements is shown in Fig. 8. These measurements were repeated several times during the experimental study: each time with another sample to catch all possible uncertainties. Thus, error bars in graphs for sputtering rates consist of all the errors above and the standard deviation.

III. RESULTS AND DISCUSSION

A. Sputtering

1. Sputtering yields

a. Experimental parameters. Plasmas' parameters applied for the sputtering are shown in Table IV.

b. Sputtering yield calculation. Calculations of the sputtering yield Y were made using measured ion flux F_{ion} and sputtered thickness Δd over time Δt . The shape of the IFEDFs for each sputtering regime was considered in the yield calculation's algorithm:

- (1) at first, sputtering yield, $Y(E_i)$, was roughly calculated assuming all ions at the energy of high energetic pick, using the formula $Y = S\rho/F_{\text{ion}}$, where Y is the sputtered yield (atoms/ions), $S = \Delta d/\Delta t$ is the "sputtering rate" (cm/s), equal to the ratio of the film thickness change Δd to the sputtering process duration Δt (Fig. 8), ρ is the atomic density calculated from a mass

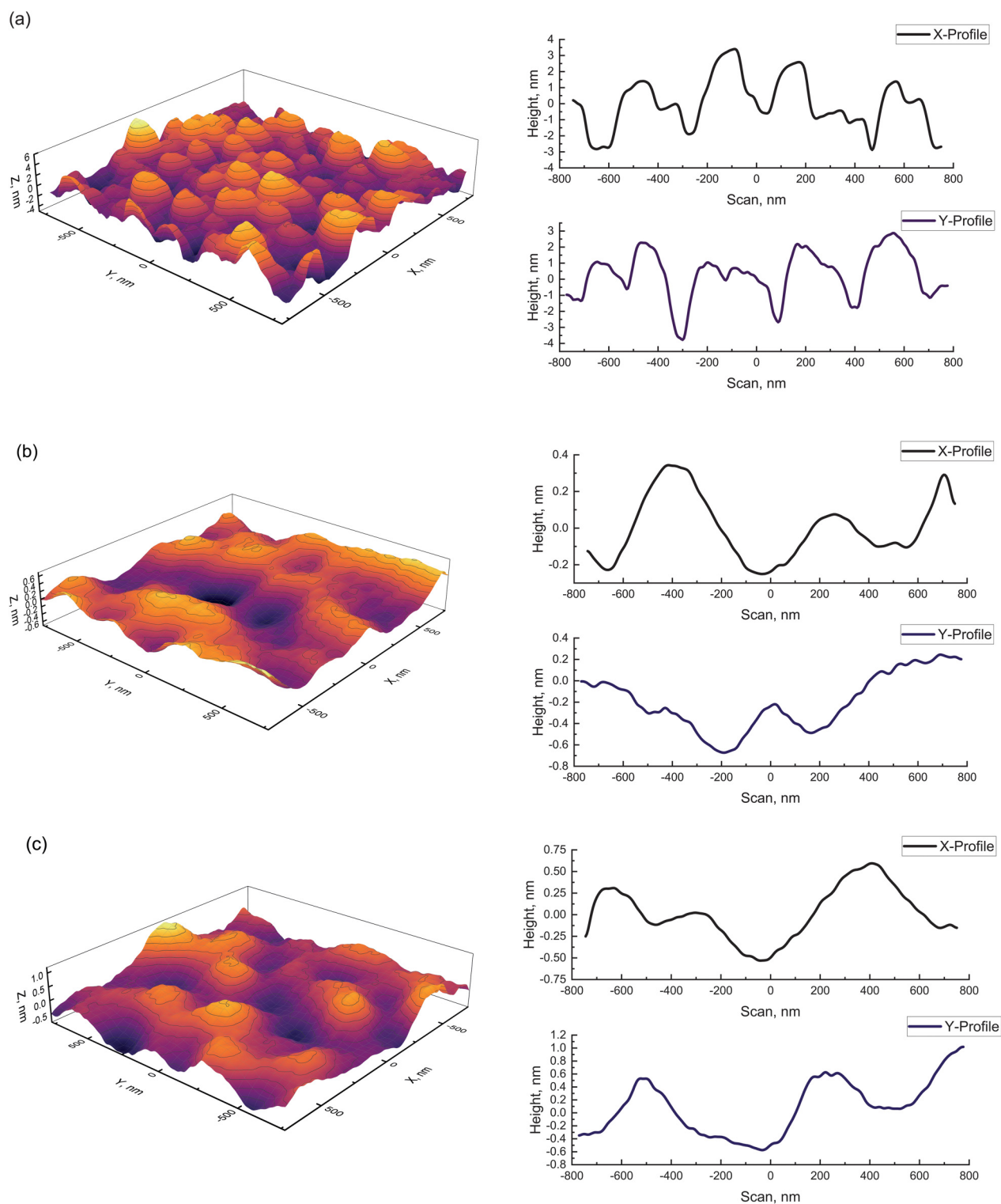


FIG. 7. Three- and two-dimensional AFM images of (a) pristine, after sputtering of top 20 nm by (b) argon and (c) xenon ions with 200 eV energy.

22 August 2023 09:06:09

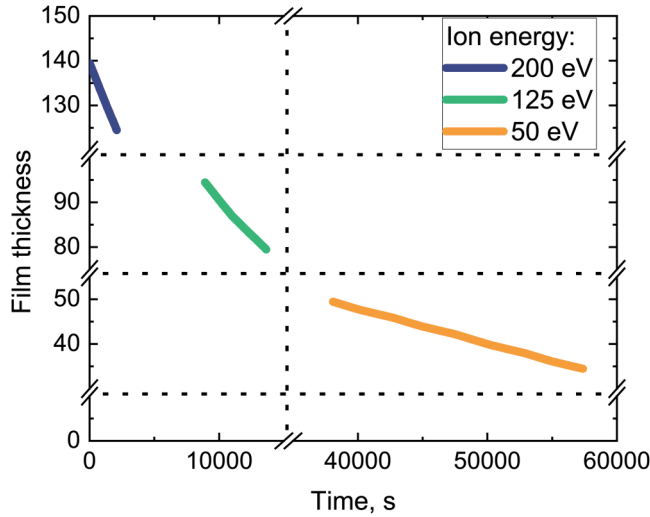


FIG. 8. The laser ellipsometry data from the sample sputtering by Ar⁺ ions at different energies. Sputtering rates *S* determined by the slopes of the lines.

density of 2.32 g/cm³ and a silicon atomic mass of 28 amu, and F_{ion} is the ion flux [ions/(cm² s)];

- (2) $Y(E_i)$ was linearly approximated at each energy interval to provide a new yield for all energies corresponding to real IFEDF's shape;
- (3) sputtering yields were recalculated using yields from the previous step and the normalized IFEDFs; and
- (4) steps (2) and (3) were repeated until the difference between the corresponding rates of two consequent iterations was less than 0.001% of the latest rate for all sputtering regimes.

c. Results. The obtained Si sputtering yields, $Y(E_i)$, for Ar⁺, Kr⁺, and Xe⁺ ions are shown in Fig. 9. As expected, the sputtering yield drops with decreasing ion energy. However, the slopes of $Y(E_i)$ are significantly changed below the energy of about 75 eV. Thus, the $Y(E_i)$ curves are visually divided into two parts: high-energy sputtering for the energies above ~75 eV and low-energy sputtering below ~75 eV.

Data for the high-energy sputtering for all studied ions demonstrate linear dependency on ion energy, while their extrapolation produces physical sputtering thresholds of about 70 ± 5 eV. The dependency slope is minimal for most heavy Xe⁺ ions and maximal for most light Ar⁺ ions, which mass is closer to the silicon atom mass. The low-energy sputtering also has linear dependencies of the sputtering rate on ion energy. However, the slope of the dependencies is significantly less than the high-energy sputtering ones.

Decreasing rather slowly, sputtering yields do not drop to zero at energies below the physical sputtering threshold, mentioned in the previous paragraph. Linear extrapolation of the $Y(E_i)$ low-energy parts to zero energy seems to show no sputtering thresholds. At least, the thresholds are too low to identify, since the magnitude of the error is comparable with the $Y(E_i)$ values in this energy range. The distinct change in the $Y(E_i)$ slope and very low thresholds indicate the change in the sputtering mechanism from “classical” kinetic or physical sputtering to a new one, which may be similar to so-called “chemical sputtering”²⁷ or “potential sputtering.”^{27,28} In plasma, in addition to ion kinetic energy, ion neutralization energy and metastable atoms’ excitation energy, as well as vacuum ultraviolet (VUV) photons from plasma, may promote the material atom removal directly or indirectly, through the surface modification and excitation relaxation. The flux of metastable atoms,^{29–31} as well as VUV photons’ flux,^{32,33} is approximately of the ions’ flux under the considered conditions. While the ion kinetic energy greatly exceeds the atom excitation energy, the classical physical sputtering (i.e., purely kinetic) is dominant. However,

22 August 2023 09:06:09

TABLE IV. Plasma parameters for the sputtering. E_{ion} —ion energy, U_{dc} —dc bias potential, F_{ion} —ion flux, P —gas pressure, and n_e —plasma electron density.

E_{ion} (eV)	Ar			Xe			Kr		
	$P = 10$ mTorr			$P = 5$ mTorr			$P = 10$ mTorr		
	$n_e = 1.47 \times 10^{10} \text{ cm}^{-3}$			$n_e = 1.15 \times 10^{10} \text{ cm}^{-3}$			$n_e = 1.25 \times 10^{10} \text{ cm}^{-3}$		
	U_{dc} (V)	F_{ion} (cm ⁻² s ⁻¹)	U_{pl} (V)	U_{dc} (V)	F_{ion} (cm ⁻² s ⁻¹)	U_{pl} (V)	U_{dc} (V)	F_{ion} (cm ⁻² s ⁻¹)	U_{pl} (V)
18	0	5.29×10^{14}	11.5	1	6.61×10^{14}	12
22	3	1.01×10^{15}	15.5
25	-1	1.01×10^{15}	15.5	-4	5.30×10^{14}	11.5	-3	6.63×10^{14}	12
50	-28	1.07×10^{15}	15.5	-31	5.34×10^{14}	12.5	-30	6.67×10^{14}	13.5
75	-53	1.14×10^{15}	16	-59	5.53×10^{14}	13.5	-57	6.86×10^{14}	14.5
100	-75	1.22×10^{15}	16.5	-84	5.72×10^{14}	14.5	-81	7.05×10^{14}	15.5
125	-98	1.26×10^{15}	17	-109	5.91×10^{14}	15.5	-105	7.24×10^{14}	16
150	-120	1.29×10^{15}	17.5	-135	6.10×10^{14}	16	-129	7.43×10^{14}	17
175	-140	1.31×10^{15}	18	-166	6.29×10^{14}	17.5	-154	7.51×10^{14}	18
200	-163	1.33×10^{15}	19	-184	6.48×10^{14}	18	-180	7.62×10^{14}	18.5

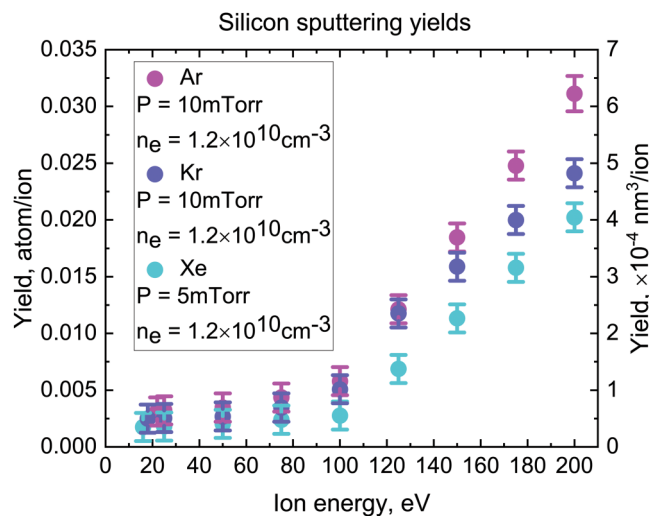


FIG. 9. Silicon sputtering yields' dependencies on ion energy by argon, krypton, and xenon ions.

at ions' energies below the kinetic sputtering threshold, the impact of other factors can also impact on the surface, modifying and reducing surface bonds and promoting atom removal due to other mechanisms, different from the kinetic one. Thus, we suggest that low-energy sputtering is a product of the complex impact of not only kinetic collisions but also ion neutralization, quenching of metastable excited atoms, and VUV photon absorption.

2. Comparison with other experiments and TRIM calculations

The comparison is presented in Fig. 10. The TRIM curve was obtained on SRIM 2003, assuming the silicon surface binding energy to be 4.73 eV.³⁴ At the chosen ions' energy region, a variation in the first decimal of the binding energy noticeably affects the calculated sputtering yield; thus, TRIM calculations presented in different studies may noticeably differ. In addition, the TRIM model had not been optimized for such low energies (mostly due to the lack of experimental data for this range); hence, the observed deviation of the obtained results from the TRIM curve is quite expected.

While there are plenty of systematic studies of silicon³⁵ (most of them with ion beams), only a few of them can be considered to have been made under reliable conditions for ion energy below 200 eV and none of them in plasma. For comparison, we selected only the experiments that had been made (a) in the similar ion energy range, (b) in a relatively clean environment (i.e., without specially added chemically active gases), and (c) with reliable and precise enough *in situ* measurements of material thickness' dynamics. Thus, it allows us to focus on comparison with the results of only two works: Varga *et al.*³⁶ and Balooch *et al.*³⁷

In the first study,³⁶ no information of the ions' flux measurements was presented. Therefore, it is impossible to validate exactly

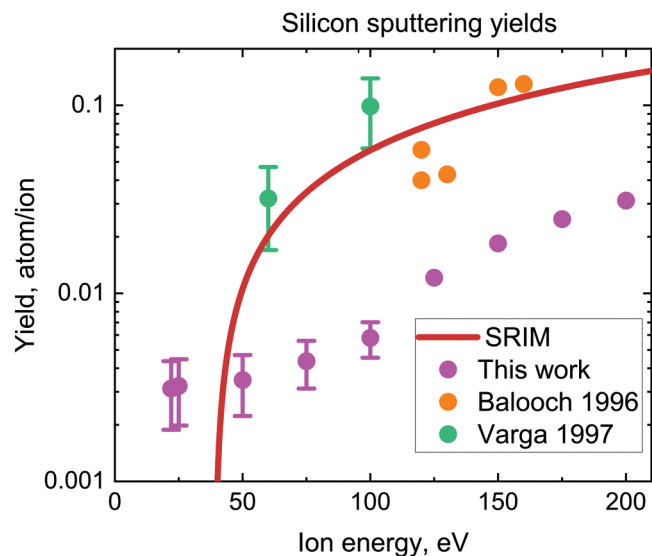


FIG. 10. Comparison of this work silicon sputtering yields by Ar⁺ ions with other works and SRIM calculations.

their yield in absolute values. In the second study,³⁷ the experimental setup removes ions with energies below selected cut-off values. The cut-off energies were slightly less than IEDF peaks, which increases mean ion energies; however, in yield calculations, the cut-off energy was considered the ion energy. At the same time, the setup may also unpredictably increase the ion angular distribution, which, together with the previous issue, could lead to the overestimation of the yields.

Accurate absolute measurement of the yield is most often difficult in experimental studies. It is one side of the “big scatter problem” for the yield at low ion energy. The other side is the possible modification of the surface due to ion bombardment. This surface modification depends on the sort of ions, ion flux, and total dose as well as ion energy and, surely, the structure of the target material. To insight somehow into this issue, we carried out a series of AFM and XPS measurements of the treated samples.

B. Surface layer

The top surface layer of pristine and sputtered by Ar⁺ and Xe⁺ ion samples was inspected by AFM and XPS, more detailed parameters of which are given in Sec. II C 1. AFM measured roughness of the pristine surface is about $\pm 2\text{--}3$ nm, while the surface roughness of the samples sputtered by Ar⁺ and Xe⁺ ions is essentially low, being about ± 0.5 and ± 0.75 nm, respectively, which clearly demonstrates the “flattening” of the material surface under ion bombardment.

To make the results more descriptive, we added the approximate depth axis together with the sinus of the angle of incidence. The approximate depth was estimated assuming the maximum XPS analysis depth of about ~ 4 nm from the Kratos Analytical Axis Ultra DLD specifications (i.e., x-ray photoelectron free path length).

22 August 2023 09:06:09

The *ex situ* XPS data demonstrate a noticeable quantity of contaminants in all the samples. The XPS data at the normal angle of incidence for the pristine silicon samples show about ~14% of carbon and ~26.7% of oxygen, while the treated samples contain a few percent of aluminum (~5.4% and ~6.4% for Ar⁺ and Xe⁺ treated, respectively) and corresponding noble gas (~1.5% of Ar and ~1.1% of Xe), as well as higher concentrations of O (~37.7% for Ar⁺ treated and ~40.4% for Xe⁺ treated) and C (~30.3% for Ar⁺ treated and ~24.2% for Xe⁺ treated). The oxygen and carbon contaminations are the result of the samples' exposure to the room atmosphere, while argon, xenon, and aluminum were deposited during sputtering. Angular analysis provides sufficient data to distinguish composition changes in the material bulk from the compounds deposited on top of the samples. The percentage of Si, O, Ar, and Xe decreases with the decrease in the angle of incidence, while Al and C concentrations essentially grow (up to two times). Considering the above, one can suppose that aluminum was partly redeposited on top of silicon from the aluminum electrode during sputtering, while carbon appeared on top of the material due to exposure to different carbon compounds (mostly organic ones) during transfer from the experimental chamber to XPS.

The material bulk contamination (just under the surface boundary) provides additional information about the modification of the silicon top layer during sputtering. Pristine and the treated

samples were approximately at the same time under atmosphere exposure; however, the percentage of O, as well as the change in the Si 2p peak intensity (Figs. 11 and 12), demonstrates a significant increase in the oxidized layer in the sputtered samples. Indeed, the sputtered samples demonstrate almost full conversion of Si-Si bonds into Si-O in the topmost layer and a significant content of oxygen in the depth, where Ar and Xe are also observed. At the same time, pristine samples demonstrate the lower content of oxygen on top, while oxygen is almost absent in the depth. It corresponds to the well-known process of silicon oxidation in the room atmosphere, i.e., so-called native oxide ~2 nm (Fig. 12). It is known that defects in silicon strongly promote oxidation. The higher the density of defects, the stronger and deeper the oxidation. Therefore, it is quite reasonable to suppose that the energetic ions penetrating into the Si bulk create defects, which then promote stronger Si oxidation under exposure to atmospheric oxygen.

The ratio of Ar and Xe to Si atoms' XPS spectra vs sinus of the angle of incidence for Ar⁺ and Xe⁺ ions sputtered samples, respectively, is shown in Fig. 13. The results can be interpreted as Ar and Xe relative to Si concentration vs depth.

The areal density N_s of Ar and Xe atoms provides additional qualifying information about possible modification of the top layer. It was estimated from the XPS data as follows: $N_s = N_A(\rho h/\mu)^i n_a$, where N_A is the Avogadro constant, ρ is the material density, h is

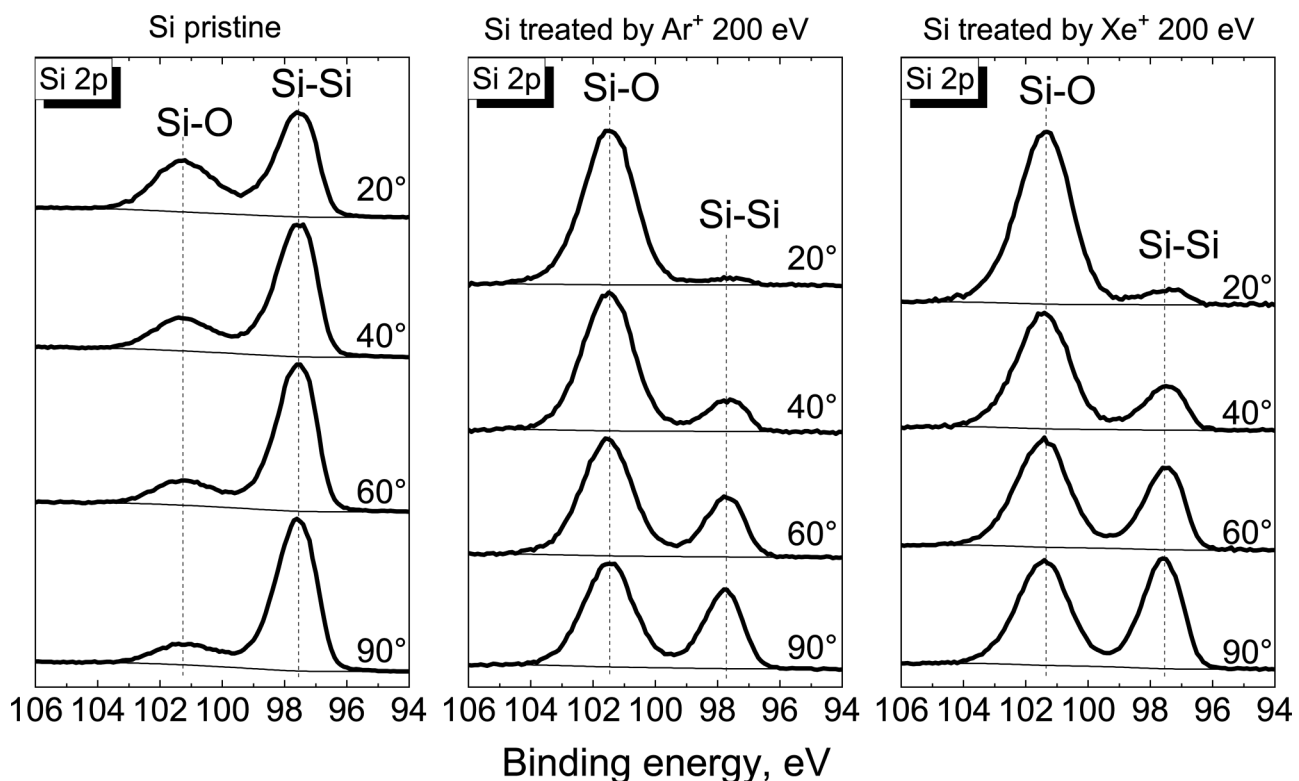


FIG. 11. Modification of Si-2p after sputtering. XPS data for different angles of incidence.

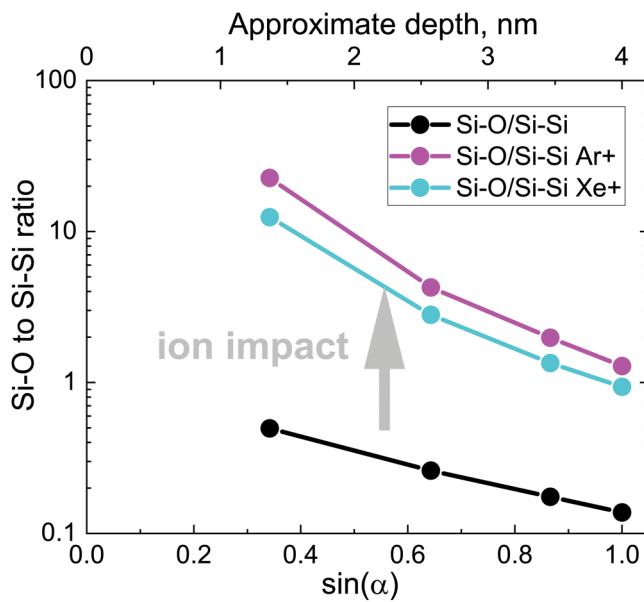


FIG. 12. Changes in the Si-O to Si-Si ratio extracted from Si 2p.

the maximum XPS analysis depth, μ is the molar mass, and n_a is the relative XPS peak intensity of implanted atoms. Estimated areal densities are $\sim 9.2 \times 10^{14}$ and $\sim 5.4 \times 10^{14}$ atom/cm² for Ar and Xe, respectively. At such doses without sufficient heating (~ 900 – 1500 °C) in standard implantation techniques (with keV–MeV ions), implanted atoms tend to form agglomerates.³⁸

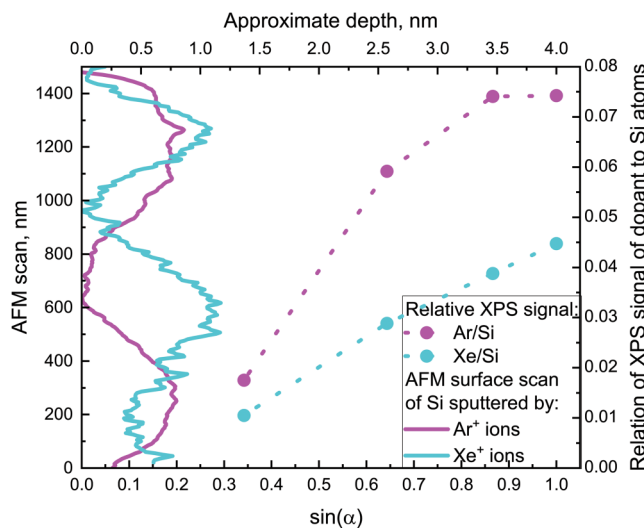


FIG. 13. Relative to silicon atom concentrations of argon and xenon atoms in the samples after sputtering by Ar⁺ and Xe⁺ ions, respectively. The surface roughness for each sample, obtained in the AFM study, is illustrated together with the XPS dependencies.

The analogous phenomenon is well known for high-energy (thousands of eV) ions in plasma, when high doses of the implanted ions lead to the formation of blisters under the surface.^{39,40} It is also observed in nanometer multilayer structures exposed to low-energy (tens and hundreds of eV) ions.^{40,41} We suppose that during sputtering, the formation of some sort of clusters of noble gases can happen on the structural irregularities, appearing due to damage by bombarding atoms of the pristine material. In this sense, the implantation of ions can lead to decreasing the sputtering yield.

IV. CONCLUSION

Sputtering of thin amorphous silicon films by Ar⁺, Kr⁺, and Xe⁺ ions at normal incidence of ions was studied in the energy range of 20–200 eV under the plasma conditions. The experiments were carried out in a low-pressure ICP discharge (~ 10 mTorr), respectively, in pure argon, krypton, and xenon at a plasma density of 1×10^{10} – 1.5×10^{10} cm⁻³. The samples were placed on a thermally stabilized electrode, with applied RF bias to control the energy of the ions arriving at the electrode. In this case, the composition, energy spectrum, and ion flux on the electrode surface were measured. The sputtering rate was measured *in situ* with a laser ellipsometer.

These measurements made it possible to accurately determine the sputtering yield $Y(E_i)$ of amorphous silicon under plasma conditions in the range of 20–200 eV. As far as we know, these are the first systematic data on $Y(E_i)$ in plasma for such low ion energies, especially for less than 70 eV. It is shown that at high ion energy, above the threshold of ~ 70 eV, the “classical” kinetic sputtering mechanism prevails, where $Y(E_i)$ rapidly grows with increasing ion energy. In this case, the sputtering yield is the lowest for heavy Xe⁺ ions and the highest for Ar⁺ ions, the mass of which is closest to the mass of target Si atoms.

As the ion energy decreases below the threshold, $Y(E_i)$ becomes low in the absolute value, but the character of the $Y(E_i)$ dependence changes. $Y(E_i)$ slowly decreases with lowering ion energy down to an energy of ~ 20 eV. This indicates a significant contribution from another “potential” sputtering mechanism. Plasma treatment including additional sources of ion surface neutralization, fluxes of excited metastable atoms, and VUV photons onto the surface may affect the surface state and, therefore, change the sputtering rate. The XPS analysis made under different angles indirectly confirms the essential modification of the Si top layers.

Thus, under plasma conditions, when large fluxes of energetic particles, in addition to the ions themselves, arrive at the surface of the treated material, it is possible to sputter the material at very low ion energy due to the modification and excitation of the surface by these particles. So, for example, the authors observed the gradual shifting of the threshold of fast “kinetic” sputtering in Ar plasma to the low energy (up to 30 eV) due to essential increasing discharge power, i.e., plasma density and fluxes of active particles on a surface, which can be indirect confirmation of such an impact. In principle, the mechanism of low-threshold potential ion sputtering may be possible without plasma itself. Anyway, it, as well as the low-energy sputtering in plasma, requires a careful study in the context of atomic layer plasma technologies.

22 August 2023 09:06:09

ACKNOWLEDGMENTS

The authors acknowledge the support from the Lomonosov Moscow State University Program of Development for providing access to the XPS facility. The authors thank Konnikova Maria (<https://orcid.org/0000-0003-4701-6483>), Department of Physics Lomonosov, Moscow State University, for providing AFM study.

AUTHOR DECLARATIONS

Conflict of Interest

The authors have no conflicts to disclose.

Author Contributions

D. R. Shibanov: Conceptualization (equal); Data curation (equal); Formal analysis (equal); Investigation (equal); Methodology (equal); Supervision (equal); Validation (equal); Visualization (equal); Writing – original draft (equal); Writing – review & editing (equal). **D. V. Lopaev:** Conceptualization (equal); Data curation (equal); Formal analysis (equal); Investigation (equal); Methodology (equal); Project administration (equal); Supervision (equal); Validation (equal); Writing – original draft (equal); Writing – review & editing (equal). **S. M. Zyryanov:** Data curation (equal); Formal analysis (supporting); Investigation (supporting); Resources (lead); Software (lead). **A. I. Zotovich:** Data curation (supporting); Formal analysis (supporting); Investigation (supporting); Resources (supporting); Software (supporting). **K. I. Maslakov:** Investigation (supporting); Methodology (equal); Resources (supporting); Validation (supporting). **A. T. Rakhimov:** Funding acquisition (lead); Project administration (equal); Resources (supporting); Supervision (equal); Validation (equal).

DATA AVAILABILITY

The data that support the findings of this study are available from the corresponding authors upon reasonable request.

REFERENCES

- W. Li, X. Zhan, X. Song, S. Si, R. Chen, J. Liu, Z. Wang, J. He, and X. Xiao, “A review of recent applications of ion beam techniques on nanomaterial surface modification: Design of nanostructures and energy harvesting,” *Small* **15**(31), 1901820 (2019).
- S. K. Höeffgen, S. Metzger, and M. Steffens, “Investigating the effects of cosmic rays on space electronics,” *Front. Phys.* **8**, 1–9 (2020).
- T. Zachs, A. Schertel, J. Medeiros, G. L. Weiss, J. Hugener, J. Matos, and M. Pilhofer, “Fully automated, sequential focused ion beam milling for cryo-electron tomography,” *eLife* **9**, 1–14 (2020).
- C. E. Ascheron and W. Skolaut, *Topics in Applied Physics Sputtering by Particle Bombardment* (Springer, Berlin, 2007).
- P. Sigmund, in *Sputtering by Particle Bombardment I. Topics in Applied Physics*, edited by R. Behrisch (Springer, Berlin, 1981), pp. 9–71.
- G. Ecke, R. Kosiba, V. Kharlamov, Y. Trushin, and J. Pezoldt, “The estimation of sputtering yields for SiC and Si,” *Nucl. Instrum. Methods Phys. Res. B* **196**(1–2), 39–50 (2002).
- V. A. Godyak, R. B. Piejak, and B. M. Alexandrovich, “Measurement of electron energy distribution in low-pressure RF discharges,” *Plasma Sources Sci. Technol.* **1**(1), 36–58 (1992).
- M. A. Bogdanova, D. V. Lopaev, S. M. Zyryanov, and A. T. Rakhimov, “‘Virtual IED sensor’ at an rf-biased electrode in low-pressure plasma,” *Phys. Plasmas* **23**(7), 073510 (2016).
- R. L. Stenzel, “Microwave resonator probe for localized density measurements in weakly magnetized plasmas,” *Rev. Sci. Instrum.* **47**(5), 603–607 (1976).
- R. B. Piejak, J. Al-Kuzee, and N. S. J. Braithwaite, “Hairpin resonator probe measurements in RF plasmas,” *Plasma Sources Sci. Technol.* **14**(4), 734–743 (2005).
- R. B. Piejak, V. A. Godyak, R. Garner, B. M. Alexandrovich, and N. Sternberg, “The hairpin resonator: A plasma density measuring technique revisited,” *J. Appl. Phys.* **95**(7), 3785–3791 (2004).
- V. Godyak, “RF discharge diagnostics: Some problems and their resolution,” *J. Appl. Phys.* **129**(4), 041101 (2021).
- D. Gahan, B. Dolinaj, and M. B. Hopkins, “Comparison of plasma parameters determined with a Langmuir probe and with a retarding field energy analyzer,” *Plasma Sources Sci. Technol.* **17**(3), 035026 (2008).
- D. Gahan, B. Dolinaj, and M. B. Hopkins, “Retarding field analyzer for ion energy distribution measurements at a radio-frequency biased electrode,” *Rev. Sci. Instrum.* **79**(3), 033502 (2008).
- D. Gahan, S. Daniels, C. Hayden, D. O. O’Sullivan, and M. B. Hopkins, “Characterization of an asymmetric parallel plate radio-frequency discharge using a retarding field energy analyzer,” *Plasma Sources Sci. Technol.* **21**(1), 015002 (2012).
- D. Gahan, S. Daniels, C. Hayden, P. Scullin, D. O’Sullivan, Y. T. Pei, and M. B. Hopkins, “Ion energy distribution measurements in rf and pulsed dc plasma discharges,” *Plasma Sources Sci. Technol.* **21**(2), 024004 (2012).
- T. H. M. Van De Ven, C. A. De Meijere, R. M. Van Der Horst, M. Van Kampen, V. Y. Banine, and J. Beckers, “Analysis of retarding field energy analyzer transmission by simulation of ion trajectories,” *Rev. Sci. Instrum.* **89**(4), 043501 (2018).
- M. Bogdanova, D. Lopaev, T. Rakhimova, D. Voloshin, A. Zotovich, and S. Zyryanov, “‘Virtual IED sensor’ for df rf CCP discharges,” *Plasma Sources Sci. Technol.* **30**(7), 075020 (2021).
- K. Köhler, J. W. Coburn, D. E. Horne, E. Kay, and J. H. Keller, “Plasma potentials of 13.56-MHz rf argon glow discharges in a planar system,” *J. Appl. Phys.* **57**(1), 59–66 (1985).
- C. Wild and P. Koidl, “Ion and electron dynamics in the sheath of radio-frequency glow discharges,” *J. Appl. Phys.* **69**(5), 2909–2922 (1991).
- T. Faraz, Y. G. P. Verstappen, M. A. Verheijen, N. J. Chittock, J. E. Lopez, E. Hejdra, W. J. H. Van Gennip, W. M. M. Kessels, and A. J. M. MacKus, “Precise ion energy control with tailored waveform biasing for atomic scale processing,” *J. Appl. Phys.* **128**(21), 213301 (2020).
- M. A. Lieberman, and A. J. Lichtenberg, *Principles of Plasma Discharges and Materials Processing*, 2nd ed. (Wiley, Hoboken, NJ, 2005), pp. 1–26.
- M. Z. Hossain, J. B. Freund, and H. T. Johnson, “Ion impact energy distribution and sputtering of Si and Ge,” *J. Appl. Phys.* **111**(10), 103513 (2012).
- M. Bogdanova, D. Lopaev, S. Zyryanov, D. Voloshin, and T. Rakhimova, “Relation between the ion flux and plasma density in an rf CCP discharge,” *Plasma Sources Sci. Technol.* **27**(2), 025003 (2018).
- P. Durgapal, J. R. Ehrstein, and N. V. Nguyen, in *The 1998 International Conference on Characterization and Metrology for ULSI Technology* (ASCE, 1998), pp. 121–131.
- R. M. A. Azzam, in *Handbook of Optics*, 3rd ed., edited by M. Bass and Optical Society of America (McGraw-Hill, 2009), pp. 1–26.
- W. Jacob and J. Roth, *Sputtering by Particle Bombardment* (Springer, Berlin, 2007), pp. 329–400.
- F. Aumayr and H. Winter, “Potential sputtering,” *Philos. Trans. R. Soc. A* **362**(1814), 77–102 (2004).
- S. Schröter, H. Bahre, M. Böke, and J. Winter, “The role of argon metastables in an inductively coupled plasma for treatment of PET,” *Plasma Processes Polym.* **11**(3), 239–246 (2014).
- A. S. Kovalev, T. V. Rakhimova, A. T. Rakhimov, O. V. Proshina, A. N. Vasilieva, and D. G. Voloshin, “Dynamics of Ar metastable and resonance

states in pulsed capacitively coupled plasmas,” *Phys. Plasmas* **28**(9), 093507 (2021).

³¹A. S. Kovalev, K. A. Kurchikov, O. V. Proshina, T. V. Rakhimova, A. N. Vasilieva, and D. G. Voloshin, “Determination of the excited argon states densities in high-frequency capacitive discharge,” *Phys. Plasmas* **26**(12), 123501 (2019).

³²M. R. Baklanov, V. Jousseau, T. V. Rakhimova, D. V. Lopaev, Y. A. Mankelevich, V. V. Afanas’ev, J. L. Shohet, S. W. King, and E. T. Ryan, “Impact of VUV photons on SiO₂ and organosilicate low-k dielectrics: General behavior, practical applications, and atomic models,” *Appl. Phys. Rev.* **6**(1), 011301 (2019).

³³J. R. Woodworth, M. E. Riley, V. A. Amatucci, T. W. Hamilton, and B. P. Aragon, “Absolute intensities of the vacuum ultraviolet spectra in oxide etch plasma processing discharges,” *J. Vac. Sci. Technol. A* **19**(1), 45–55 (2001).

³⁴Y. Kudriavtsev, A. Villegas, A. Godines, and R. Asomoza, “Calculation of the surface binding energy for ion sputtered particles,” *Appl. Surf. Sci.* **239**(3–4), 273–278 (2005).

³⁵Y. Yamamura and H. Tawara, “Energy dependence of ion-induced sputtering yields from monatomic solids at normal incidence,” *At. Data Nucl. Data Tables* **62**(2), 149–253 (1996).

³⁶P. Varga, T. Neidhart, M. Sporn, G. Libiseller, M. Schmid, F. Aumayr, and H. P. Winter, “Sputter yields of insulators bombarded with hyperthermal multiply charged ions,” *Phys. Scr.* **T73**, 307–310 (1997).

³⁷M. Balooch, M. Moalem, W. Wang, and A. V. Hamza, “Low-energy Ar ion-induced and chlorine ion etching of silicon,” *J. Vac. Sci. Technol. A* **14**(1), 229–233 (1996).

³⁸J. F. Ziegler, *Ion Implantation Science and Technology* (Elsevier, 1988).

³⁹A. S. Kuznetsov, M. A. Gleeson, and F. Bijkerk, “Ion effects in hydrogen-induced blistering of Mo/Si multilayers,” *J. Appl. Phys.* **114**(11), 113507 (2013).

⁴⁰M. Goorsky, *Ion Implantation* (InTech, 2012).

⁴¹R. A. J. M. van den Bos, C. J. Lee, J. P. H. Benschop, and F. Bijkerk, “Blister formation in Mo/Si multilayered structures induced by hydrogen ions,” *J. Phys. D: Appl. Phys.* **50**(26), 265302 (2017).